Submitted to the 29th International Conference on High-Energy Physics ICHEP98,
Vancouver, Canada, July 1998

Determination of the Gluon Density in the Proton from Charm Electro- and Photo-Production using NLO QCD

H1 Collaboration

Abstract

With the H1 detector at the ep collider HERA, D^* meson production cross sections have been measured in deep inelastic scattering with 4-momentum transfers $Q^2 > 2$ GeV$^2/c^2$ and in photo-production at energies $W_{\gamma p} \approx 88$ and 194 GeV. Next-to-Leading Order QCD calculations are found to describe the differential cross sections well, both in shape and in normalization. Using these calculations, the NLO gluon momentum distribution in the proton, $xg(x)$, has been extracted in the momentum fraction range $7.5 \cdot 10^{-4} < x < 4 \cdot 10^{-2}$, at average scales $\mu^2 = 25$ to 50 GeV$^2/c^2$. The gluon momentum fraction x has been obtained from the measured kinematics of the scattered electron and the D^* meson in the final state. The results compare well with the gluon distribution obtained from the analysis of scaling violations of the proton structure function F_2.

Abstract: 538
Parallel sessions: 4, 7
Plenary sessions: 6, 9

1 Introduction

The most precise determinations of the gluon momentum distribution in the proton have been obtained so far from the analysis of scaling violations of the deep inelastic proton structure function F_2 [1, 2]. This method is however indirect in the sense that F_2 at low values of the Bjorken scaling variable x_B actually probes the sea quark distributions which are related via the QCD evolution equations to the gluon distribution. The local behaviour of F_2 depends on the gluon distribution $x_g g(x_g)$ in a rather wide range of momentum fractions x_g, and the analysis requires the assumption of a certain functional form of $x_g g(x_g)$, the parameters of which are then determined in a fit procedure.

More direct determinations of the gluon density can be obtained by partial reconstruction of the kinematics of the interacting partons from the measurement of the hadronic final state in gluon-induced processes. Such direct measurements are complementary to the indirect analyses: although limited in statistics, they are in principle more sensitive to local variations of the gluon distribution. They are affected by different systematics and provide an independent test of the underlying concepts. Direct gluon density determinations have previously been performed using dijet events [3, 4].

The production of heavy quarks in electron proton interactions proceeds, in QCD, almost exclusively via photon gluon fusion, where a photon coupling to the incoming electron interacts with a gluon in the proton by forming a quark-anti-quark pair. Total and differential charm photo-production cross sections were found to be well reproduced by such a description in Next to Leading Order (NLO) QCD [5], and the same holds for the charm contribution to the proton structure function, $F_2^{c\bar{c}}$ [6, 7, 8].

Compared to the jet case, smaller invariant masses of the partonic sub-process can be accessed in charm production. It is thus possible to extend the gluon density determination towards smaller momentum fractions x_g. Also, there is much less background from quark-induced processes.

Recently, Next-to-Leading-Order (NLO) QCD calculations of fully differential charm cross sections at HERA have become available, both for deep inelastic scattering (DIS), where the negative squared 4-momentum transfer from the scattered electron $Q^2 \gtrsim 1$ GeV^2 [9, 10], and for the photo-production regime [11, 12], where Q^2 is almost zero. In the analyses presented here, these calculations are used to determine $x_g g(x_g)$ directly in NLO from the measurement of differential D^* production cross sections with the H1 detector. The theoretical framework and the principle of the analysis will be described in more detail in the next section. In Section 3 the measurement of differential $D^\star$ production cross sections will be presented separately for DIS and photo-production, and the results will be compared with predictions based on the NLO QCD calculations. Section 4 will explain the method to extract the gluon density and present the results. The article concludes with a comparison of these with results obtained by H1 from the analysis of F_2.

2 Principle of the Analysis

Differential charm production cross sections in ep interactions have been calculated [11, 12, 13] in NLO QCD in the $\overline{\text{MS}}$ renormalization scheme. The computations were carried out using the subtraction method, which is based on the replacement of divergent soft and collinear terms in the squared matrix elements by generalized distributions. Charm quarks are treated as massive particles appearing only in the final state whereas the three light flavours (and gluons) are the only active partons in the initial state ("Three Flavour Number Scheme"). In leading order, the production proceeds via the partonic sub-process $\gamma g \to c\bar{c}$. In NLO, there are in addition diagrams where a gluon is radiated from a gluon or a quark line, $\gamma g \to c\bar{c}g$, and quark induced processes $\gamma q \to c\bar{c}q$ and $\gamma\bar{q} \to c\bar{c}\bar{q}$.

Since the calculations are fully differential, they provide access to the 4-vectors of all outgoing partons. The evaluation of cross sections can be performed using Monte Carlo integrators. The calculations by Harris and Smith for DIS have been implemented in the HVQDIS program [10], those for the photo-production case by Frixione *et al.* in the FMNR package [12]. These techniques also allow the effect of charm quark fragmentation into D^* mesons to be modelled. This is performed in the programs by a convolution of the charm quark cross section with the Peterson fragmentation function [14]; the D^* 3-momentum vector is formed by scaling the quark 3-momentum vector, and the D^* energy is fixed such that the mass is $m(D^*) = 2.01$ GeV/c^2. Evolution of the fragmentation function, which one expects to become important for transverse momenta $p_\perp \gg m_c$, is not included because the region of interest is $p_\perp \sim m_c$ ($m_c =$ charm quark mass). In this framework, visible cross sections (incorporating experimental cuts) can be calculated in NLO as a function of any final state variable depending on the D^* and electron 4-momenta. The cross sections can then be confronted with experimental data at the hadron level.

The kinematics of the leading order $2 \to 2$ process $\gamma g \to c\bar{c}$ is fully determined if one incoming and one outgoing particle, here the photon and the charm (anti-)quark, are measured. The momentum fraction x_g is given by

$$x_g = \frac{M^2 + Q^2}{y \cdot s} \quad \text{with} \quad M^2 = \frac{p_{\perp c}^{*2} + m_c^2}{z(1-z)} \quad \text{and} \quad z \equiv \frac{p \cdot p_c}{p \cdot q} = \frac{(E - p_z)_c^{\text{(Lab)}}}{2yE_{\text{beam}}} \;, \tag{1}$$

where $p^*_{\perp c}$ is the transverse momentum of the charm quark in the photon proton centre of mass frame with respect to the axis defined by the incoming proton momentum in this frame. z is a Lorentz invariant that can be evaluated in the laboratory frame from the charm quark's energy E and momentum component p_z.[1] p, q, and p_c denote the 4-momenta of the incoming proton, exchanged photon, and outgoing (anti-)charm quark, respectively. $Q^2 = -q^2$ and $y = (2p{\cdot}q)/s$; $\sqrt{s}$ is the ep centre of mass energy, and E_{beam} the electron beam energy in HERA. In DIS, x_g is related to the Bjorken scaling variable via $x_g = x_B(1 + M^2/Q^2)$.

In the presence of gluon radiation (or a gluon transverse momentum in the initial state), relation (1) holds only approximately. Also, in the experiment one measures not quarks but D^* mesons that carry only a fraction of the c quark's energy. However, with the replacements

$$p^*_{\perp c} \to 1.2\, p^*_{\perp D^*} \;, \quad (E - p_z)_c \to (E - p_z)_{D^*} \;, \quad x_g \to x_g^{OBS} \tag{2}$$

one can construct a hadronic observable x_g^{OBS} that is well correlated with x_g. The factor 1.2 compensates for the average fraction of charm quark momentum carried by the D^* meson.

The calculation of the visible cross section $\sigma(x_g^{OBS})$ can be written as

$$\sigma(x_g^{OBS}) = \int_{x_{g,min}}^{1} dx_g \; \left[g(x_g, \mu^2) \cdot \hat{\sigma}(x_g^{OBS}, x_g, \mu^2) \right] + \sigma_{quark}(x_g^{OBS}) \tag{3}$$

[1] H1 uses a right-handed coordinate system with the z axis defined by the incident proton beam, and the y axis pointing upward.

where μ is the factorization scale and $\hat{\sigma}$ plays the role of a partonic cross section, which is integrated over the remaining kinematic degrees of freedom and also depends on the experimental acceptance. It receives the dominant contributions from regions where $x_g \approx x_g^{OBS}$. σ_{quark} denotes the quark-induced contribution to the visible cross section. The form of Equation 3 is such that a determination of the gluon density in the proton can be made from the measured cross section by means of an unfolding procedure.

In photo-production, the small virtuality allows the photon to fluctuate into a hadronic state and therefore behave as a hadron in the interaction with the proton. Such processes are called resolved photon processes in contrast to the direct case where the photon is pointlike. While the resolved process is known to be important for the light quark production, it is expected that the direct part is dominant for charm production in the visible phase space (where at least one charmed meson is produced in the detector acceptance). Previous measurements of charm photo-production [5] have confirmed this. It is thus a good approximation to treat the resolved contributions as a systematic uncertainty.

The analysis proceeds in two main steps. First, the visible D^* cross section is measured as a function of x_g^{OBS}. The data are corrected only for detector effects to the hadron level. As there is no extrapolation into unmeasured regions needed nor are there any parton hadron correlations involved, this step can be performed using the leading order Monte Carlo programs which describe the final state well. To establish our confidence in the reliability of the theory, the resulting cross sections are confronted with the NLO QCD predictions.

In the second step the cross section is unfolded to the true variable x_g and the gluon density $x_g g(x_g, \mu^2)$ is extracted. This step is carried out in NLO QCD in the framework of the Three Flavour Number Scheme. The programs HVQDIS and FMNR are used to calculate the cross sections as a function of x_g^{OBS} as well as the correlations used for the unfolding from hadronic to partonic quantities, taking into account gluon radiation and fragmentation effects.

3 Cross Section Measurement

The data used here have been collected with the H1 detector during the 1994 to 1996 running period of the HERA collider, where 27.5 GeV positrons (henceforth generically termed "electrons") collided with 820 GeV protons, at a centre of mass energy of $\sqrt{s} = 300$ GeV.

The H1 detector and its trigger capabilities have been described in detail elsewhere [15]. Charged particles are measured by two cylindrical jet drift chambers [16, 17], mounted concentrically around the beam-line inside a homogeneous magnetic field of 1.15 Tesla, yielding particle charge and momentum from the track curvature in the polar angular range of $20° < \theta < 160°$, where θ is measured with respect to the incident proton beam direction. Two double layers of cylindrical multi-wire proportional chambers (MWPC) [18] with pad readout for triggering purposes are positioned inside and in between the two drift chambers, respectively. The tracking detector is surrounded by a fine grained liquid argon calorimeter [19], consisting of an electromagnetic section with lead absorbers and a hadronic section with steel absorbers. It covers polar angles between 4° and 155°. In the backward region, it is complemented by a lead scintillator "Spaghetti" calorimeter (SpaCal) [20] which is optimized for the detection of the scattered electron in the DIS kinematic range under consideration. It consists of an electromagnetic and a coarser segmented hadronic section. The measurement of the scattering angle is improved by a four-layer drift chamber (BDC) [21] mounted on its front. The luminosity is determined from the rate of *Bethe-Heitler* $ep \to ep\gamma$ bremsstrahlung events. The luminosity system consists of an electron detector and a photon detector, located 33 m and 103 m from the interaction point in the electron beam direction, respectively. The electron detector at 33 m, referred to by *ETAG33*, is used to tag photo-production events by detecting electrons scattered at small angles. In 1995 and 1996 a second electron tagging detector of the same type was added at 44 m, which extends the y-range to much lower values. In the analyses below it will be referred to as *ETAG44*. Due to their different y-ranges, both electron detectors cover a different $W_{\gamma p}$ regime, and thus are complementary. A time-of-flight system (TOF) is located in the backward direction at $z \approx -2$ m.

The reconstruction of D^* mesons follows closely that in the previously published measurement of D^* photo-production [5]. It makes use of the D^* tagging technique [22], *i.e.* of the tight kinematical conditions in the in the decay chain $D^{*+} \to D^0\pi^+_{slow} \to (K^-\pi^+)\pi^+_{slow}$[2] for which the overall branching ratio is $BR(D^* \to K\pi\pi)$= 2.62% [23]. Particle tracks passing the quality cuts of Ref. [5] and fulfilling transverse momentum cuts depending on the kinematic range, were considered as K and π candidate in turn (no particle identification is applied). The invariant mass of the $K\pi$ combination had to be consistent with the D^0 mass within ± 80 MeV/c^2. D^{*+} production is found as a distinct enhancement in the distributions of the mass difference $\Delta M = M(K^-\pi^+\pi^+_{slow}) - M(K^-\pi^+)$ around the expected mass difference of 145.4 MeV/c^2. The ΔM distributions for all D^* candidates are shown in Fig 1 for the DIS (a) and the two photo-production samples (b,c). No enhancement is observed if the mass difference for the wrong charge combinations $M(K^-\pi^-\pi^+) - M(K^-\pi^-)$ is used instead.

The number of events, N_{D^*}, is extracted from Likelihood fits to the distributions of the mass difference with a function taken to be a superposition of a Gaussian for the signal and a term $N_B(\Delta M - m_\pi)^a$ for the background. The position and width of the Gaussian are fixed to the values found from the total sample including photo-production and DIS events. The position is consistent with the table value [23], and the width agrees with simulation results. The normalization of the signal, the background normalization N_B and shape exponent a are free parameters in the fit. Other methods of determining the number of candidates have also been applied and yield the same numbers within the statistical errors. Uncertainties from variations of the fit procedure are accounted for in the systematic error. From Monte Carlo simulations the contribution to the signal in DIS due to D^0 decays into channels other than $K^-\pi^+$, is obtained to be $r = (7 \pm 4)\%$, for which a correction is made.

A Monte Carlo simulation is used to determine the efficiency for the reconstruction, the selection cuts, and the acceptance of the detector. Hard scattering events for electro-production and for direct and resolved photo-production are generated in leading order with the AROMA 2.2 [24] and PYTHIA 5.7 programs [25]. The generated events are then fed into the H1 detector simulation program, and are subjected to the same reconstruction and analysis chain as the real data. The observed rapidity and transverse momentum distributions of D^* mesons are acceptably reproduced. The changes found when using in DIS a rather soft Peterson fragmentation function ($\epsilon = 0.100$) as compared to the Lund fragmentation were accounted for in the systematic error. The dependence of the simulated efficiencies on other choices made for the simulation (charm mass, parton density distributions) was estimated to be small and was neglected.

Differential cross sections as functions of kinematic variables are measured by dividing the data sample into bins and determining the numbers of D^* mesons and the efficiencies in each

[2]The charge conjugate is always implied.

bin using the fit and correction procedure as above, for each data taking period separately. The effect of limited detector resolution on the x_g^{OBS} and the other variables is small with respect to the chosen bin sizes.

In the **DIS analysis**, the cross section for the process $ep \rightarrow eD^*X$ has been measured in the visible range $2 < Q^2 < 100$ GeV^2, $0.05 < y < 0.7$, $p_\perp(D^*) > 1.5$ GeV/c and $|\eta(D^*)| < 1.5$, where $\eta = -\ln\tan(\theta/2)$ is the pseudo-rapidity.

The data have been taken in the years 1995-96, after the installation of the SpaCal and BDC. They correspond to a total integrated luminosity of $\mathcal{L} = 9.69$ pb^{-1}. The events have been triggered by an electro-magnetic cluster in the SpaCal [20] of at least 6.5 GeV energy, mostly in coincidence with a charged track signal from the MWPC and central drift chamber trigger.

The identification of electrons is similar to the procedure used in the inclusive structure function measurement [26]. Electrons are identified as clusters in the SpaCal with energy $E_e >$ 8 GeV, with a cluster radius <3.5 cm consistent with electro-magnetic energy deposition, and with a cluster centre matched by a charged track candidate in the backward drift chamber [21] within 2.5 cm. The scattering angle was required to be $\theta_e < 177^o$. The Deep Inelastic Scattering kinematic variables are reconstructed using the "$e\Sigma$ method" [27]

$$Q^2 = 4E_{\text{beam}}E_e\cos^2\frac{\theta_e}{2} \quad \text{and} \quad y = \frac{2E_{\text{beam}}\sum_{had}(E-p_z)}{\left[\sum_{all}(E-p_z)\right]^2} \quad , \tag{4}$$

where the sum in the denominator runs over all (liquid Argon and SpaCal) calorimetric signals as well as central drift chamber tracks, avoiding double counting. The sum in the numerator is over all calorimeter signals except those forming the scattered electron candidate. y can also be measured using the electron alone ("e method"),

$$y_e = 1 - (E_e/E_{\text{beam}})\sin^2(\theta_e/2) \quad , \tag{5}$$

or using the hadronic final state alone, $y_\Sigma = (\sum_{had}(E-p_z)/2E_{\text{beam}}$. The energy distribution of the scattered electron as well as the ratio y_Σ/y_e are well described by the Monte Carlo simulation. The results obtained with both methods were found to be in very good agreement. The $e\Sigma$ method needs smaller radiative corrections. It is quite robust against uncertainties in the electron energy and was used for the 95 data. For the 96 data, the e method was used.

For D^* reconstruction, transverse momentum cuts of $p_\perp > 300(120)$ MeV$/c$ have been imposed on the K and π (π_{slow}) candidates. In order to suppress combinatorial background, the range of z (Eqs. 1,2) has been restricted to $z > 0.2$ for $p_\perp(D^*) < 3$ GeV$/c$. Variations found by applying or not applying this cut are accounted for in the systematic error.

A total of $N_{D^*} = 591 \pm 35$ events is observed. The efficiency for electron and D^* reconstruction and selection is found to be ϵ_{reco} =42% on average, ranging from 34% in the lowest to 57% in the highest x_g^{OBS} bin. The trigger efficiency has been determined from data, by using independent trigger conditions. It is found to be ϵ_{trig} =98.6% (83.3%) on average for the 95 (96) running period. The dependence on the event kinematics is small and has been taken from simulations.

There is no indication of photo-production background seen in the data; the electron energy and y_Σ distributions are consistent with expectations for a pure sample of DIS events. From simulations of direct and resolved charm photo-production, we expect less than 1 event within the cuts specified. No subtraction is therefore made and a 1% error attributed to this possible background source.

Contributions from $b\bar{b}$ production, with subsequent decays of b flavoured hadrons into D^* mesons, has been calculated using the AROMA generator to be about $N_B = 10$ events in total and has not been subtracted. The systematic error on the inclusive $D*$ cross section assigned to this accounts for the variation of the efficiency due to a variation of the $b\bar{b}$ contribution within a factor of 5 of its predicted value.

Radiative corrections have been calculated using the analytic program HERACLES [28]. They amount to $\delta_{rad} = 3\%$ (7%) on average for the $e\Sigma$ (e) method.

The cross section for the given range in Q^2, y, $p_\perp$ and η is obtained as

$$\sigma_{vis} = \frac{N_{D^*}(1-r)}{\epsilon_{trig}\epsilon_{rec}\, BR(D^* \to K\pi\pi)\, \mathcal{L}\, (1+\delta_{rad})} = (5.62 \pm 0.33 \pm 0.95)\mathrm{nb}\ , \tag{6}$$

where the first error is statistical, the second is systematic. The largest contribution ($7.5\,\%$) is due to the uncertainty in the track reconstruction. Other important sources of systematic errors include uncertainties in the trigger efficiency, in the D^* signal extraction, in the modeling of the D^* distributions, and in the radiative corrections. All contributions show only slight variation with x_g^{OBS}.

In [7, 8] the cross section results are shown as function of $p_\perp(D^*)$, $p_\perp^*(D^*)$, $\eta(D^*)$, Q^2, and x_B and found to be in good agreement with NLO QCD.

The **photo-production analysis** is carried out independently for the case where the scattered electron is detected in the electron tagger at 33 m (*ETAG33*) and in the tagger at 44 m (*ETAG44*). Henceforth, the respective data samples will be referred to as *ETAG33* and *ETAG44* sample. The total integrated luminosities of these samples are $10.7\ \mathrm{pb}^{-1}$ for *ETAG33* and $10.2\ \mathrm{pb}^{-1}$ for *ETAG44*. There is no overlap between them.

The events were triggered by a coincidence of the *ETAG* signals with track candidate signals obtained from the MWPC and central drift chamber trigger systems. Proton beam induced background is reduced by requiring the event vertex to lie within ± 40 cm of the nominal interaction point along the beam direction. A further reduction is achieved by excluding events with energy flow only into the forward region of the detector.

The full kinematical range for the D^{*+}-candidates within which the differential distributions are measured is chosen to be a rapidity within $-1.5 < \eta^*(D^{*+}) = -\frac{1}{2}\ln\frac{E-p_z}{E+p_z} < 1.5$ and a transverse momentum above $2.5\,\mathrm{GeV/c^2}$ for the *ETAG33* sample and $2.0\,\mathrm{GeV/c^2}$ for the *ETAG44* sample. The analysis is restricted to the kinematical region $0.29(0.02) < y = 1 - E_{e'}/E_e < 0.62(0.32)$ and $Q^2 < 10^{-2}\,(0.009)\,\mathrm{GeV}^2$ for the *ETAG33* (*ETAG44*) sample.

Correspondingly, the γp CM energy range is limited to 162 GeV$< W_{\gamma p} < 234$ GeV, with a mean of $\overline{W_{\gamma p}} = 194$ GeV and an average $\langle Q^2 \rangle \approx 10^{-3}$ GeV^2. The acceptance of the electron tagger *ETAG33* is above $20\,\%$ with an average value of about $60\,\%$ in this range. For the *ETAG44* the scattered electron energy cannot be determined accurately enough, hence an averaged value for the acceptance is used. The acceptance of the *ETAG44* peaks sharply around $y = 0.09$ and corresponds to an (acceptance-) average of $\overline{W_{\gamma p}} = 88$ GeV.

The acceptances of the electron tagger and their trigger efficiencies are accounted for by assigning weights to individual events, year- and run-range dependent for *ETAG33*, for *ETAG44* an average value is used. The method of *equivalent event numbers* [29] has therefore been used to determine acceptance-weighted numbers of D^* candidates. The K and π candidates used in the D^* reconstruction were required to have transverse momenta $p_t > 0.5$ GeV$/c$ (*ETAG33*) or

$p_t > 0.35$ GeV$/c$ (*ETAG44*) respectively, on the slow pion track a cut of $p_t > 0.15$ GeV$/c$ was imposed. 489 ± 92 (for *ETAG33*) and 299 ± 75 (for *ETAG44*) weighted combinations are found.

Using the efficiencies for the track component of the trigger condition, as well as the D^* reconstruction and selection efficiencies as determined by Monte Carlo simulations, the cross sections for the specified ranges are found using Eq. 6. Radiative corrections are negligible here. No correction was made for contributions from B decays, either. They were estimated using the AROMA Monte Carlo, taking the preliminary H1 measurement of an unexpectedly large beauty photo-production cross section [30] into account, and found to be small and included in the systematic error. The other systematic errors are the same as in the DIS analysis, except for those related to the electron measurement. They are combined in quadrature to $\pm 15\,\%$.

At $Q^2 \approx 0$, in the *Weizsäcker-Williams Approximation* (WWA) [31] the electro-production cross section σ_{ep} is expressed as a convolution of the flux of photons emitted by the electron with the photo-production cross section. The photo-production cross sections have thus been obtained with $\sigma(\gamma p \to D^{*\pm}X) = \sigma_{vis}(ep)/F$, where F is the Weizsäcker-Williams photon flux factor.

The measured distributions $1/(2B_{c\to D^{*+}}) \cdot d\sigma(\gamma p \to D^{*\pm}X)/dp_t$ (for the rapidity range of $-1.5 < \eta^* < 1.5$) are shown in Figure 2b,d. The results from both taggers cannot be combined because they cover different $W_{\gamma p}$ ranges. The distribution $1/(2B_{c\to D^{*+}}) \cdot d\sigma(\gamma p \to D^{*\pm}X)/d\eta^*$ (integrated over the range $2.5(2.0) < p_t(D^*) < 10\,GeV/c$ is shown for *ETAG33*(*ETAG44*) in Fig. 2a,c. In addition, for *ETAG33* the double-differential distribution $1/(2B_{c\to D^{*+}}) \cdot d^2\sigma(\gamma p \to D^{*\pm}X)/d\eta^* dp_t$ is presented for three different ranges of transverse momentum in Fig. 3.

The superimposed histograms shown in figures 2 and 3 represent the absolute predictions of the NLO QCD calculation [12], using a charm mass $m_c = 1.5$ GeV/c^2. The factorization and renormalization scales are given by $\mu_F = 2\mu_R = 2\sqrt{m_c^2 + p_t^2}$. The calculations are shown for the parton densities MRSA' (proton) in combination with GRV-HO [33] and LAC1 [34] (photon). The histograms for the *ETAG33* sample are averages of calculations done at three representative $W_{\gamma p}$ values, weighted by the photon flux integrated over the represented range. For *ETAG44* the calculation was performed at a fixed $\overline{W_{\gamma p}} = 88\ GeV$. Good agreement is observed for both the shape and the absolute normalization between the measured p_t and η^* distributions and the NLO QCD calculation, in particular in the low p_t region (see Fig. 3) where the bulk of the events is found, and where the QCD calculation is expected to describe most reliably the data. This provides confidence that one can extract the gluon density from this data set.

4 Determination of the Gluon Density

The gluon density in the proton is extracted from the measured cross sections $d\sigma/d(\log x_g^{OBS})$ which are compared to the NLO QCD predictions in Fig 4. The calculation for the DIS case was done with the HVQDIS program version 1.1 [10] using a charm mass $m_c = 1.5$ GeV/c^2. The QCD factorization and renormalization scales were set to $\mu = \sqrt{4m_c^2 + Q^2}$. The parton density set CTEQ4F3 [35] was used, which is consistent with the Three Flavour Number Scheme as implemented in HVQDIS and was shown in [10] to yield results very close to those obtained with the GRV 94 HO set [36]. It is preferred for the subsequent analysis since the value $\Lambda^{(5)} = 225$ MeV used yields the world average for the strong coupling constant, $\alpha_s(M_{\rm Z}) = 0.118 \pm 0.003$ [23]. For the $c \to D^*$ fragmentation fraction, the value 0.27 was used, consistent with the average value of $0.71 \pm 0.05\%$ for the fragmentation and decay chain $c \to D^{*+} \to K^-\pi^+\pi^+$ [37]. The fragmentation parameter $\epsilon_c = 0.060$ was used as determined [38] from data. This is one of the parameter settings used by the authors in Ref. [10].

The photo-production data (Fig 4b-d) are analyzed separately at three different photon-proton energies (88, 185, and 223 GeV), and the rapidity range has been restricted to $-1.5 \leq \eta \leq 0.5$ (for *ETAG33*) and $0 \leq \eta \leq 1$ (for *ETAG44*). From the NLO calculation, the resolved photon contribution in this range is expected to be less than five percent and accounted for in the systematic error.

First, according to Eq. 3 the quark-induced contribution as predicted in the QCD calculation is subtracted from the data bin by bin. It is at the percent level; the correlation with the gluon density via QCD evolution can be neglected here, but the uncertainty arising from it will be included in the error.

The quark-subtracted cross sections are converted into cross section distributions as function of true x_g using the iterative unfolding procedure for binned distributions of Ref. [39]. As an example, the correlation between x_g^{OBS} and x_g as obtained from the QCD calculation for DIS is shown as a two-dimensional histogram in Fig. 5. This correlation is used for the first unfolding iteration; for each next iteration it is re-weighted using the result of the previous one. After 4 steps at most, convergence is reached, and the "smeared" distribution $\sigma(x_g^{OBS})$ agrees with the measurement.

The unfolded cross section distribution factorizes:

$$\sigma(x_{g,i}) = g(x_{g,i}, \mu_i^2) \cdot \tilde{\sigma}(x_{g,i}) \; ; \tag{7}$$

but for every bin in x_g (and W) the gluon density is probed at another factorization scale μ_i ($\tilde{\sigma}$ is a partonic cross section). The scale in the DIS measurement changes from 17 GeV^2 in the first to 28 GeV^2 in the last bin, the average being $\bar{\mu}^2 = 4m_c^2 + \langle Q \rangle^2 = 25$ GeV^2. In photo-production, the scale varies between 30 and 140 GeV^2, with an average value of 50 GeV^2, as can be seen in Fig. 6, where $g(x_g)$ as determined from the photo-production data, is plotted as a function of the scale μ associated to the x_g and W range of each measurement. To determine $g(x, \bar{\mu}^2)$ at an average scale, all data points are scaled to this average $\bar{\mu}^2$:

$$g(x_{g,i}, \mu_F^2) = \frac{g(x_{g,i}, \bar{\mu}^2)^{\text{theory}}}{g(x_{g,i}, \mu_i^2)^{\text{theory}}} \cdot \frac{g(x_{g,i}, \mu_i^2)^{\text{theory}}}{\sigma(x_{g,i})^{\text{theory}}} \cdot \sigma(x_{g,i})^{\text{experiment}} \tag{8}$$

Whereas the $\tilde{\sigma}(x_{g,i})$ are strictly independent of $g(x_g)$, Eq. 8 also contains the variation of $g(x_{g,i}, \mu^2)$ when varying the scale from μ_i to $\bar{\mu}$. This is taken from theory, assuming the same scale dependence as in CTEQ4: The variation is however small: in the DIS measurement $g(x, \mu_i^2)$ deviates from $g(x, \bar{\mu}^2)$ by no more than 9%. The effect is included in Eq. 8, and the dependence on the input parton density scale variation is accounted for in the systematic error.

Systematic uncertainties affecting the gluon density extraction are determined by re-calculating with the QCD programs for different parameter choices the correlations and cross sections and re-analyzing the data starting from the measured cross section. In the DIS case, the QCD factorization and renormalization scale μ was varied between $2m_c$ and $2\sqrt{4m_c^2 + Q^2}$ in DIS, following [10], and the charm quark mass m_c between 1.3 and 1.7 GeV/c^2. One of the large uncertainties is due to our ignorance of the charm fragmentation function which has not yet been measured in ep scattering. It is assumed that this can be taken from measurements in

e^+e^- annihilation. A fragmentation parameter ϵ_c range between 0.020 (as recently argued [40] for NLO calculations in the "massive charm" scheme) and 0.100 was allowed in the HVQDIS calculation (0.078 was obtained from a combination of ARGUS and CLEO results [23]). The uncertainty in the strong coupling constant (world average) is taken into account by variation of the scale $\Lambda^{(5)}$ between 176 and 248 MeV [23]. In order to assess the dependence on the gluon density in the input parameterization, the MRS(D0') (already ruled out by HERA data [1, 2]) and MRS(A') sets[3] were used as extreme choices. In photo-production, the scale variation was a factor 2 in both directions. The charm quark mass, being strongly correlated with the scale, has not been varied separately here. $\epsilon_c = 0.035 \pm 0.010$, as obtained from a study of e^+e^- annihilation data within the same framework [41], was used in FMNR. In photo-production, an additional error of $^{-4\%}_{+0\%}$ accounts for resolved contributions and the uncertainty in the photon structure function. The dominant contribution in the DIS case arises from the uncertainty in the charm quark mass; at the higher x_g points, fragmentation uncertainties become important as well. For the photo-production results, the scale variation dominates over the whole range.

The resulting gluon distribution, $x_g g(x_g)$, is shown in Fig 7a, for the DIS case at the average scale of $\mu_F^2 = 25$ GeV^2. The covariance matrix for the statistical uncertainty is given in Table 1. The inner error bars in the figure represent the diagonal elements only. The correlation coefficients (defined as $\rho_{ij} = \mathrm{cov}_{ij}/\sqrt{\mathrm{cov}_{ii}\mathrm{cov}_{jj}}$) are 25%, 34%, 48% for the first, second and third pair of neighbouring bins, respectively.

Table 1: *Covariance matrix for $x_g g(x_g)$. The first 4 rows and columns correspond to the 4 bins shown in Fig 7; correlations with the adjacent bin at high x_g are also included.*

3.475				
0.347	0.535			
0.068	0.152	0.361		
0.026	0.048	0.119	0.173	
0.027	0.048	0.083	0.088	0.047

An overall normalization uncertainty is induced by the experimental systematic error of the D^* cross section, increased by the additional uncertainty from the $c \to D^*$ fragmentation fraction, and it is added (in quadrature) to the statistical error to give the total experimental error shown as outer error bars. The downward extension of the error bar finally represents the change to be applied linearly, if a $b\bar{b}$ contribution to the D^* cross section of 5 times the predicted size would have been subtracted before unfolding. The contributions to the systematic error due to variations in the parameters of the theoretical model are added in quadrature and displayed as shaded histogram along the abscissa in Fig 7a. The errors at small x_g are dominated by the statistical uncertainty.

The corresponding result from the photo-production analysis is shown in Figure 7b for the average scale of $\mu_F^2 = 50$ GeV^2. The error bars display the statistical error and the contributions to the systematic error, added linearly.

The extracted gluon densities are in very good agreement with each other, as can be seen in Fig. 8, where they are both shown at $\mu_F^2 = 25$ GeV^2. They can be compared with other measurements determined in NLO from other processes. For example, the result of the QCD analysis of

[3]These sets are not consistent with the Three Flavour Number Scheme and are used only for practical purposes here.

the scaling violations of F_2 for $x_g g(x_g)$ as obtained by H1 [42] is overlaid as well in Fig 8. This result has been obtained from a fit to a fully inclusive structure function measurement, using the NLO QCD evolution equations. Within errors it agrees well with the gluon distributions determined in the analyses presented herein,which were performed in the framework of the Three Flavour Number Scheme for DIS as implemented in the HVQDIS program, and in the "massive charm" calculations for photo-production, implemented in the FMNR program. This represents a non-trivial confirmation of the applied QCD concepts and of the universality of the parton distributions.

5 Conclusion

Using explicit NLO QCD calculations, the gluon density in the proton, $xg(x)$ has been determined from measured differential D^* cross sections in deep inelastic ep scattering at an average scale $\mu^2 = 25$ GeV^2, and in photo-production at $\langle\mu^2\rangle = 50$ GeV^2. The gluon momentum fraction x_g has been approximated to x_g^{OBS} using the kinematic information from the D^* meson in addition to the scattered electron, and the visible cross section has been measured as a function of x_g^{OBS}. $xg(x)$ has been extracted in the "massive" Three Flavour Number Scheme as implemented in the HVQDIS and FMNR programs, which use the Peterson form of the fragmentation function to model the non-perturbative hadronization process. The errors are dominated by the statistical uncertainty.

The overall description of the differential cross sections by the NLO QCD calculations has been found to be good. The extracted gluon densities agree well with each other and with the one obtained from the QCD analysis of the inclusive measurement of the proton structure function F_2.

Acknowledgements

We are grateful to the HERA machine group whose outstanding efforts have made and continue to make this experiment possible. We thank the engineers and technicians for their work in constructing and now maintaining the H1 detector, our funding agencies for financial support, the DESY technical staff for continual assistance, and the DESY directorate for the hospitality which they extend to the non-DESY members of the collaboration. We wish to thank S. Frixione, B. Harris and J. Smith for assistance in the QCD calculations and many fruitful discussions.

References

[1] S. Aid *et al.* (H1 Collaboration), Nucl. Phys. B470 (1996) 3.

[2] M. Derrick *et al* (ZEUS Collaboration), Z. Phys. C72 (1996) 399;
M. Botje, QCD Analysis of ZEUS 1994 F_2 data, in Proceedings "Workshop on Deep Inelastic Scattering and Related Phenomena (DIS 97)", Chicago, April 1997.

[3] S. Aid *et al* (H1 Collaboration) Nucl. Phys. B449 (1995) 3.

[4] K. Rosenbauer, A direct Determination of the Strong Coupling Constant and the Gluon Density in the Proton in next-to-leading-order from (2+1)-Jet Rates in the H1-Experiment, in Proceedings "Workshop on Deep Inelastic Scattering and Related Phenomena (DIS 96)", Roma, April 1996.

[5] S. Aid *et al* (H1 Collaboration), Nucl. Phys. B472 (1996) 32.

[6] C. Adloff *et al* (H1 Collaboration), Z. Phys. C72 (1996) 593;
J. Breitweg *et al* (ZEUS Collaboration), Phys. Let. B 407 (1997) 402.

[7] C. Adloff *et al* (H1 Collaboration), contributed paper Nr. 275 to the International Europhysics Conference on High Energy Physics, August 1997, Jerusalem, Israel.

[8] C. Adloff *et al* (H1 Collaboration), contributed paper to this conference (Abstract 540).

[9] B.W. Harris, hep-ph/9608379, talk A05057 presented at the 1996 annual meeting of the Division of Particles and Fields, American Physical Society, Minneapolis, MN, August 1996. To appear in proceedings thereof.

[10] B.W. Harris and J. Smith, preprint DESY 97-111, FSU-HEP-970527, May 1997.

[11] P. Nason, S. Dawson, and R.K. Ellis, Nucl.Phys. B303 (1988) 607;
R.K. Ellis and P. Nason, Nucl.Phys. B312 (1989) 551;
J. Smith and W.L. Van Neerven, Nucl.Phys. B374 (1992) 36.

[12] S. Frixione et al., Phys.Lett. B348 (1995) 633; Nucl.Phys. B454 (1995) 3.

[13] B.W. Harris and J. Smith, Nucl. Phys. B452 (1995) 109; Phys. Lett. B353 (1995) 535.

[14] C. Peterson, D. Schlatter, I. Schmitt, and P.M. Zerwas, Phys. Rev. D 27 (1983) 105.

[15] I. Abt *et al* (H1 Collaboration) Nucl. Instr. Meth. A386 (1997) 310 and 348.

[16] J. Bürger et al., Nucl.Instr.Meth. A279 (1989) 217.

[17] I. Abt et al. (H1 Coll.), Phys.Lett. B328 (1994) 176.

[18] K. Müller et al., Nucl.Instr.Meth. A312 (1992) 457.

[19] B. Andrieu et al., Nucl.Instr.Meth. A336 (1993) 460.

[20] R.D. Appuhn *et al* (H1 SpaCal group), DESY preprint 96-171.

[21] H1 collaboration, Technical proposal for the upgrade of the backward region of the H1 detector, DESY internal report PRC-93/02.

[22] G. Feldmann et al., Phys. Rev. Lett. 38 (1977) 1313.

[23] R.M. Barnett *et al* (Particle Data Group), Phys. Rev. D54 (1996) 1.

[24] G. Ingelman, J. Rathsman and G.A. Schuler, Comput. Phys. Commun. 101 (1997) 135.

[25] T. Sjöstrand, CERN-TH-6488 (1992), Comp. Phys. Comm. 82 (1994) 74.

[26] C. Adloff *et al* (H1 Collaboration), Nucl. Phys. B497 (1997) 3.

[27] U. Bassler and G. Bernardi, Nucl. Instrum. Meth. A361 (1995) 197.

[28] A. Kwiatkowski, H. Spiesberger, and H.J. Mohring, Comput. Phys. Commun. 69 (1992) 155.

[29] G. Zech, DESY preprint 95-113 (1995)

[30] U. Langenegger (H1), talk given at "Rencontres de Moriond, QCD", Les Arcs, France, March 1998.

[31] C.F. Weizsäcker, Z.Phys. 88 (1934) 612;
E.J. Williams, Phys.Rev. 45 (1934) 729.

[32] A.D. Martin, R.G. Roberts and W.J. Stirling, Phys. Lett. B354 (1995) 155.

[33] M. Glück, E. Reya, and A. Vogt, Phys. Rev. D45 (1992) 3986, D46 (1992) 1973.

[34] A. Levy, H. Abramowicz and K. Charchula, Phys. Lett. B269 (1991) 458.

[35] H. Lai *et al*, Phys. Rev. D 55 (1997) 1280.

[36] M. Glück, E. Reya, and A. Vogt, Z. Phys. C67 (1995) 433.

[37] ALEPH, DELPHI, L3 and OPAL Collab., Nucl. Instrum. Meth. A378 (1996) 101.

[38] J. Chrin, Z. Phys. C 36 (1987) 163.

[39] G. D'Agostini, Nucl. Instrum. Meth. A362 (1995) 487.

[40] M. Cacciari and M. Greco, Phys. Rev. D55 (1997) 7134.

[41] C. Oleari, private communication

[42] V. Chekelian, DESY preprint 97-248 (1997).

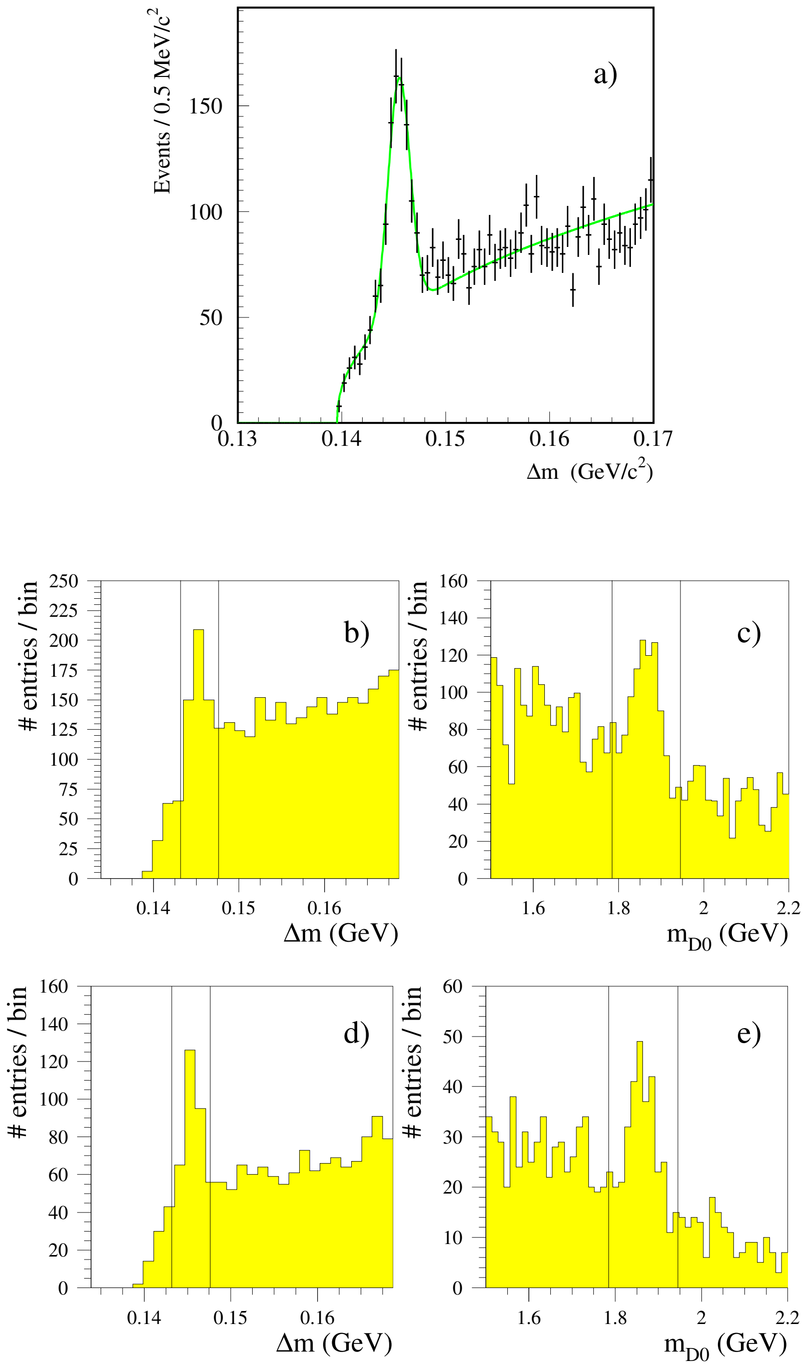

Figure 1: *Mass difference $\Delta M = M(K^-\pi^+\pi^+_{slow}) - M(K^-\pi^+)$ distribution of D^* candidates in DIS (a), and for the photo-production samples ETAG33 (b) and ETAG44 (d), where also the $M(K^-\pi^+)$ distributions are shown (c,e). The solid line in (a) represents the result of a fit as described in the text.*

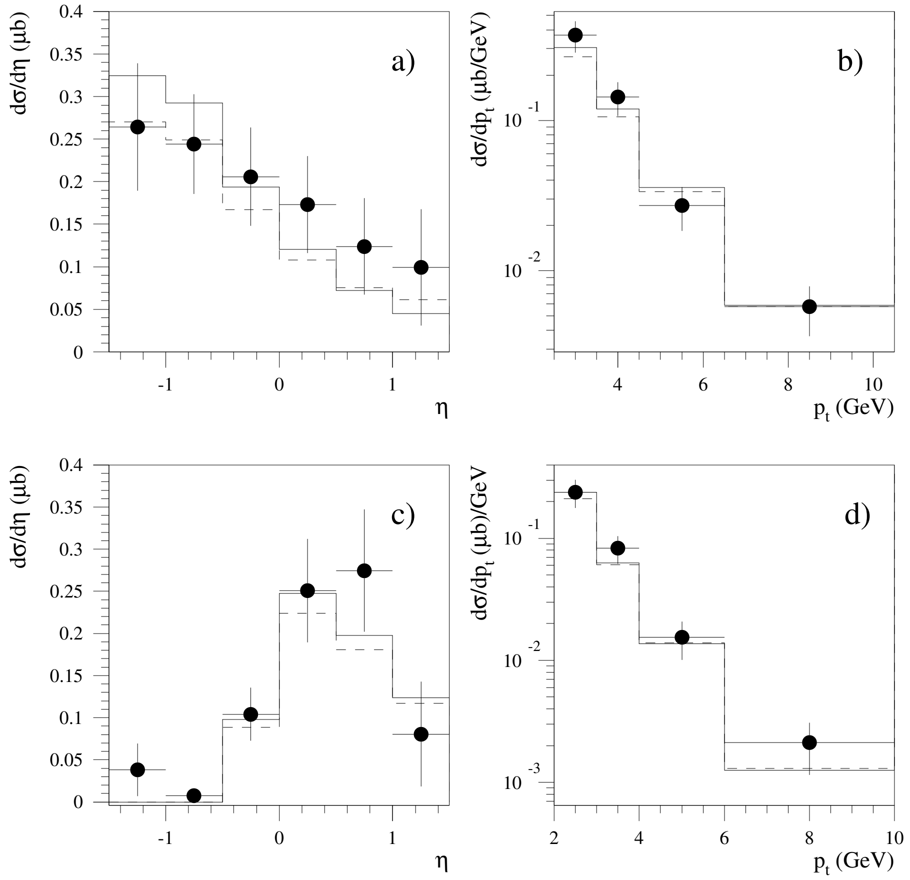

Figure 2: *Differential cross sections for the ETAG33 sample at an average $W_{\gamma p} = 194$ GeV (a,b) and for the ETAG44 sample at $W_{\gamma p} = 88$ GeV (c,d) (solid dots). (a,c) $1/(2B_{c \to D^{*+}}) \cdot d\sigma(\gamma p \to D^{*\pm}X)/d\eta^*$ for events with $p_t(D^*) > 2.5$ GeV/c (top, bottom: 2.0 GeV/c); (b,d) $1/(2B_{c \to D^{*+}}) \cdot d\sigma(\gamma p \to D^{*\pm}X)/dp_t$ for events with $-1.5 < \eta^*(D^*) < 1.5$. The histograms show the NLO QCD predictions based on the FMNR program, using the MRSG (solid) and MRSA' (dashed) proton parton density parameterization with a charm quark mass of 1.5 GeV/c^2.*

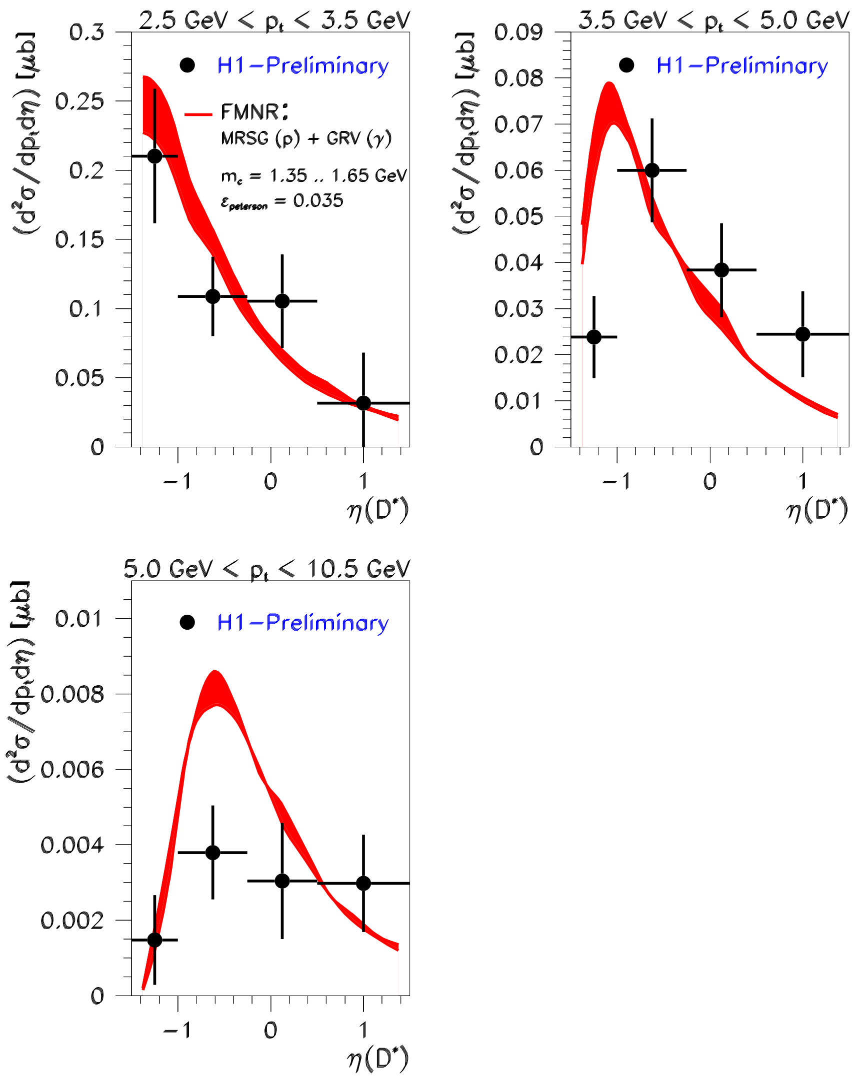

Figure 3: *Double-differential distribution* $1/(2B_{c\to D^{*+}})\cdot d^2\sigma(\gamma p\to D^{*\pm}X)/d\eta^* dp_t$ *is presented for three different ranges of transverse momentum for ETAG33. The bands represent the NLO QCD predictions based on the FMNR program and show the variations due to a variation of the charm quark mass.*

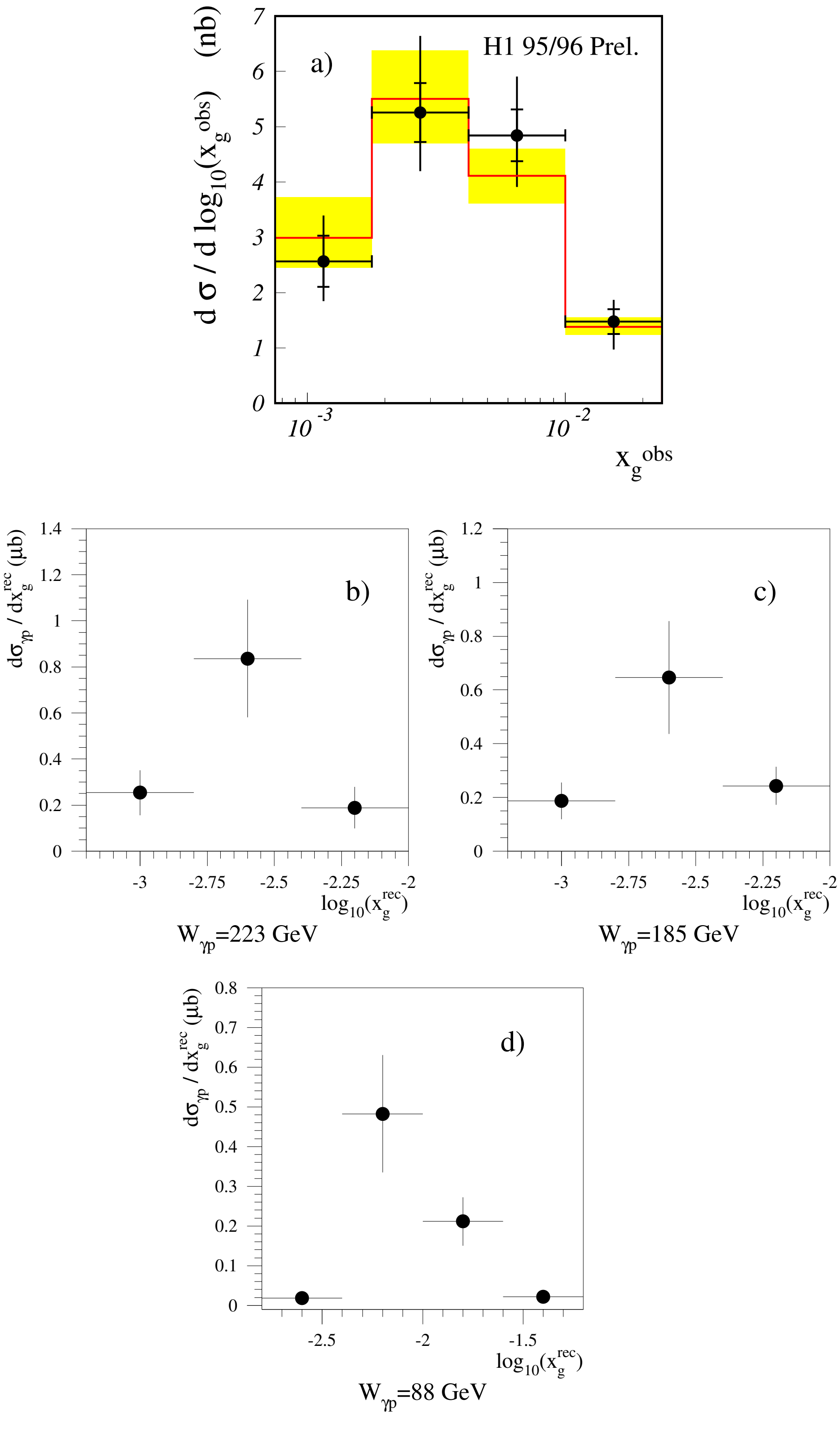

Figure 4: *(a) Differential cross section $\sigma(ep \to eD^{*}X)$ as function of x_g^{OBS} in the visible range (see text). The H1 data are shown as points with error bars, the NLO QCD prediction using the CTEQ4F3 parton distribution set is shown as a solid histogram. The shaded band represents the variation of the cross sections due to a variation of m_c between 1.3 (upper) and 1.7 GeV$/c^2$ (lower edge). Figures (b-d) show the same distributions for photo-production, separately for W =223, 185 and 88 GeV, respectively.*

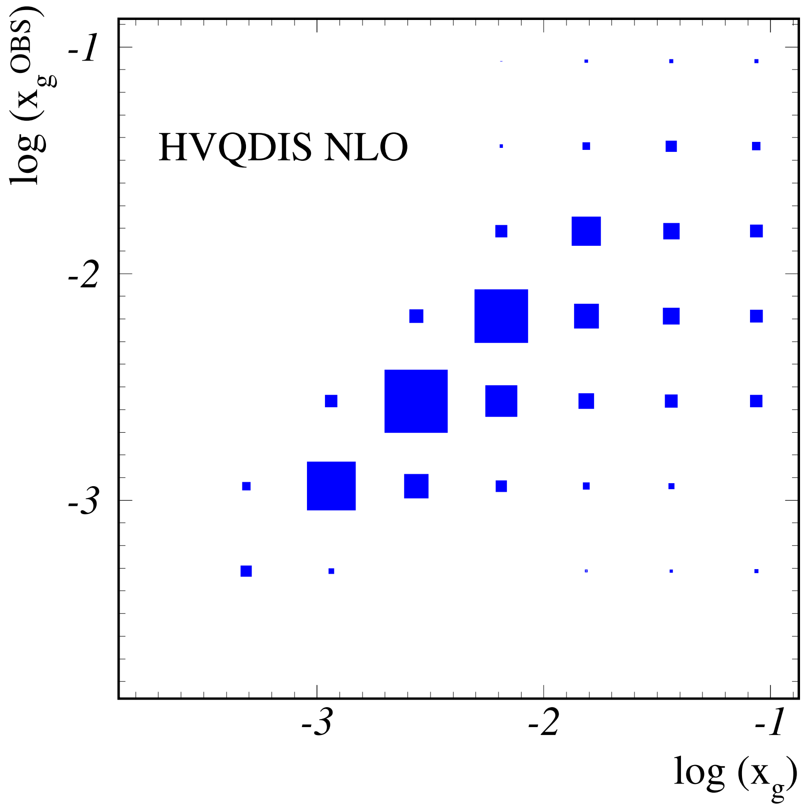

Figure 5: *Correlation between x_g^{OBS} as reconstructed from the D^* and electron momenta, and true momentum fraction x_g as predicted in NLO QCD. The bin area corresponds to the cross section contribution from the x_g interval to the measured x_g^{OBS} range. The correlations are determined by the effects of gluon radiation and fragmentation.*

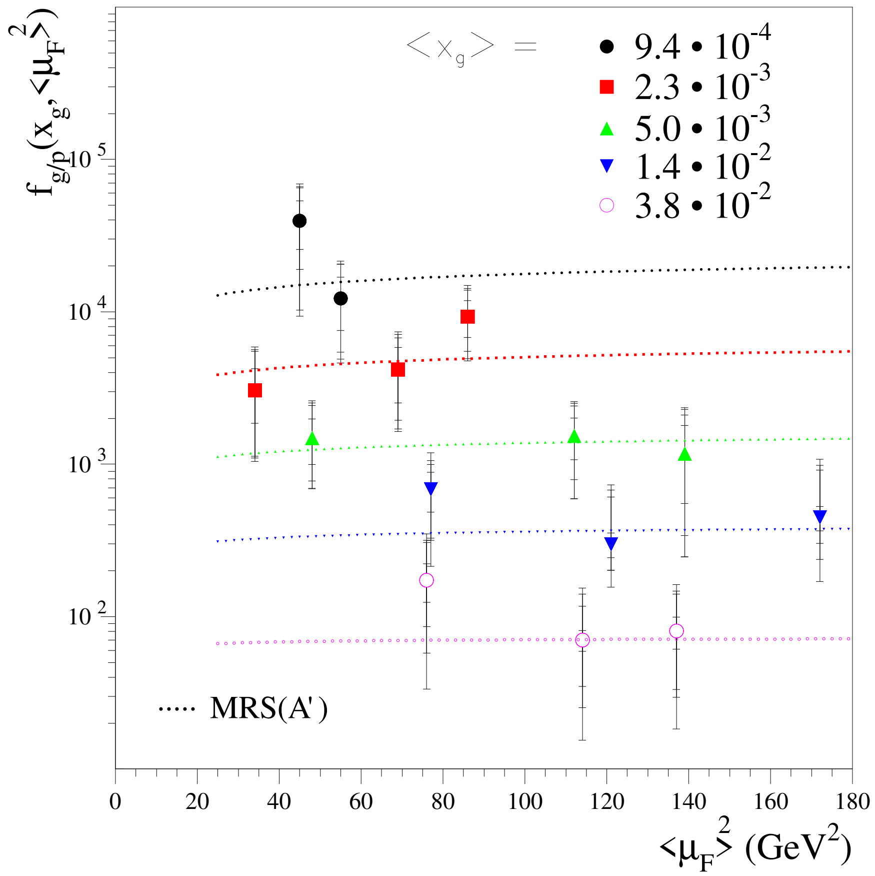

Figure 6: *Gluon density distribution, measured in photo-production as a function of the scale μ^2. Each key symbol represents a different bin in x_g with the average value given in the upper right corner. The innermost error bars are the statistical errors. The second error bars represent the scale dependence, the third ones the dependence upon the fragmentation function parameter ϵ and the outermost error all other theoretical systematic errors. All errors are added linearly. A common experimental systematic error of 15 % is not shown. The dotted lines represent the gluon density of the MRS(A') parameterization, shown as function of scale μ for the same set of x_g values. The lowest curve corresponds to the highest x_g.*

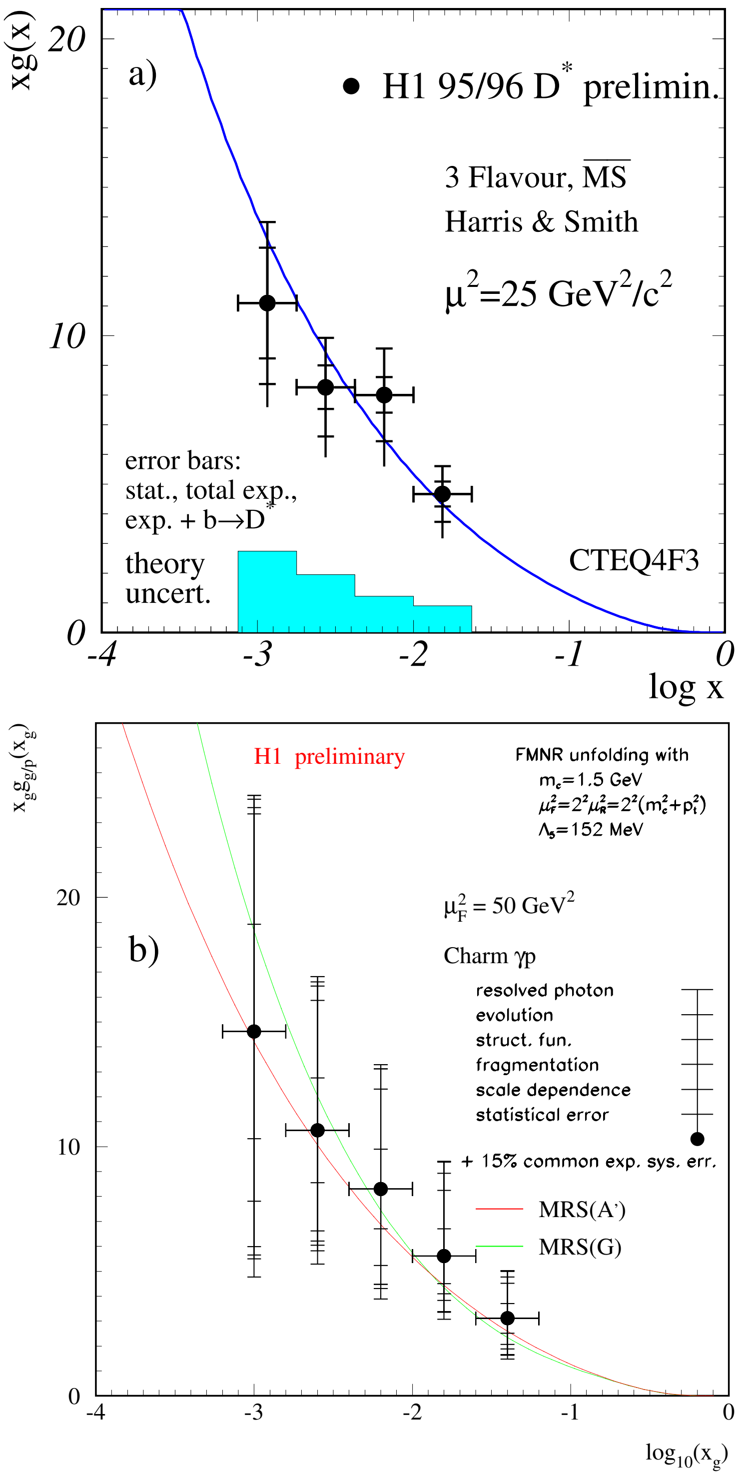

Figure 7: *(a) Gluon density, determined from DIS data, compared to the CTEQ4F3 parameterization at* $\mu^2 = 25$ *GeV*^{2}*/c*^{2} *(full line). The error bars represent the statistical (inner) and total experimental (outer) error; in addition the effect of a linear subtraction of* $b\bar{b}$ *background (if 5 times higher than expected) is displayed. The theoretical systematic error is shown as shaded band along the abscissa. (b)Gluon density distribution at an average scale of* $50\ GeV^2$*, determined from photo-production data, using the NLO QCD calculations implemented in the FMNR program. The innermost error bars are the statistical errors. The second error bars represent the scale dependence, the third ones the dependence upon the fragmentation function parameter* ϵ *and the outermost error are all other theoretical systematic errors. For illustration, all errors are added linearly. A common experimental systematic error of* $15\ \%$ *is not shown. The lines represent the gluon density of the MRS(A') and MRS(G) parameterization.*

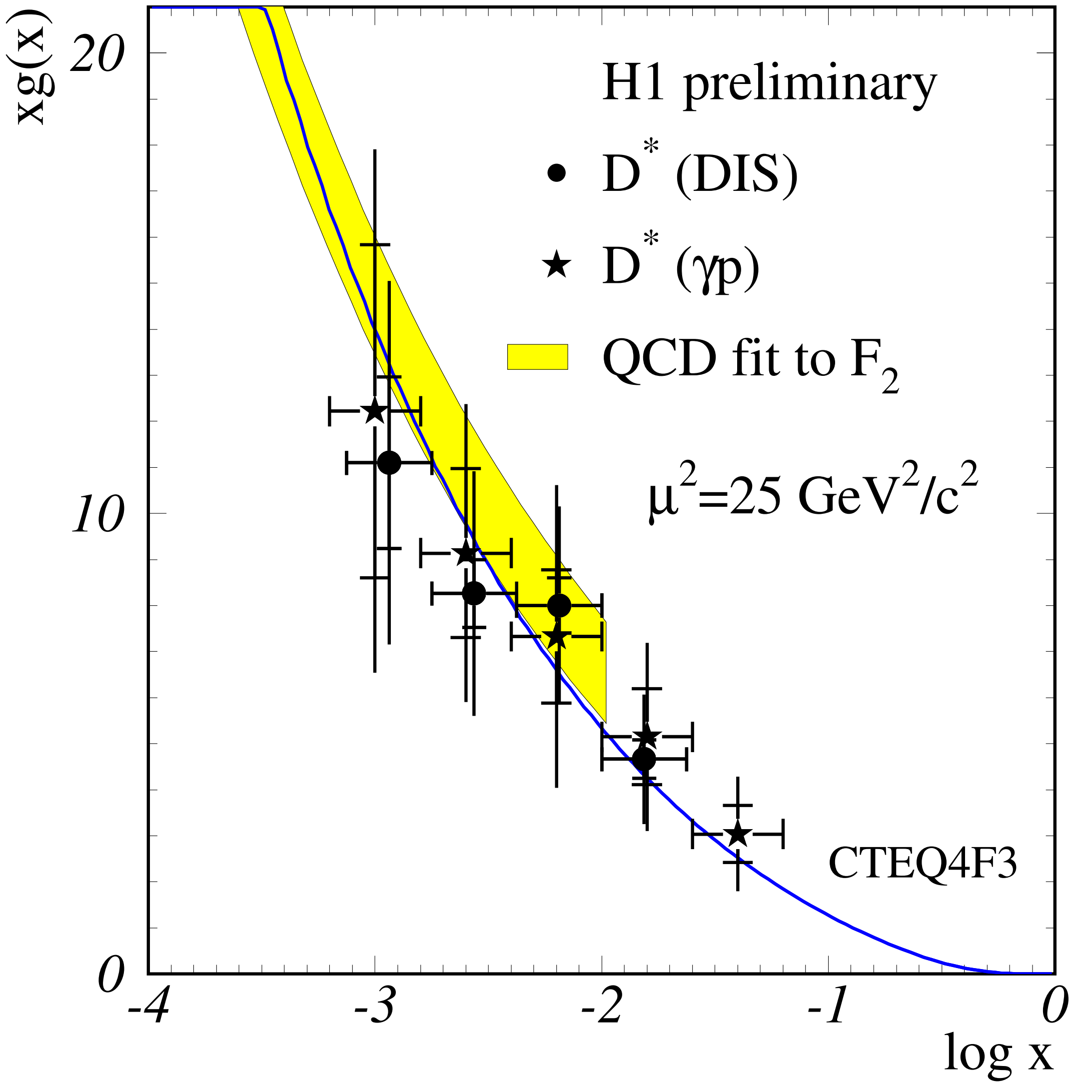

Figure 8: *Comparison of the gluon densities obtained from the two D^* analyses. The systematic error is a quadratic sum of all contributions, dominated by the uncertainty of the charm quark mass and the fragmentation parameter. Both are compared to to the result of the H1 QCD analysis of the inclusive F_2 measurement at $\mu^2 = 25$ GeV^2/c^2 (light shaded band) and the CTEQ4F3 parameterization.*